

ATLAS Internal Note
LARG-NO-88
December 1997

Copper-Polyimide Multi-Layer Electrodes for the End-Cap Electromagnetic Calorimeter

F. Djama
*CPPM,
163, Avenue de Luminy,
Case 907, 13288-Marseille, France.*

L. Hervas, C. P. Marin
*CERN,
CH-1211 Geneva 23, Switzerland.*

Abstract

The ATLAS liquid argon electromagnetic calorimeters will make use of large copper-polyimide electrodes. This note describes the geometry, the electrical properties and the mechanical interfaces of the end-cap electrodes.

1 Introduction

The end-caps of the liquid argon electromagnetic calorimeter will consist of two concentric wheels, covering pseudorapidity ranges between 1.375 and 2.5 for the outer wheel, and between 2.5 and 3.2 for the inner one. The wheels will be made of radially superposed lead absorber plates and copper-polyimide electrodes [1]. Following the conventions defined in [2], the inner wheel electrodes will be called “C”, while the outer wheel ones will be referred to as “D”.

The electrodes must be bent to fit the accordion shape of the absorbers. In the end-cap region, the folds are radial. In order to be able to obtain a wheel while stacking absorbers and electrodes, the folding angle varies along the folds, and becomes sharper when moving towards large radii [3].

External geometry and mechanical interface of both electrodes are described in section 2. Granularity, sampling depths, and cell drawing are shown in section 3, while the electrical properties are discussed in section 4.

2 The overall geometry

Computation of the dimensions of the folded electrodes at liquid argon temperature, using the η coverage (1.375-2.5, 2.5-3.2), the front z position (3702 mm), and the depth of the active volume (510 mm) is straightforward (figures 1-a and 2-a).

The flat drawing of the active area of the electrodes at room temperature is derived taking into account the number of waves (6 for electrode C and 9 for D), the curvature radius (3.25 mm for C and 3 mm for D), the variable folding angle [3] and the coefficient of thermal expansion of the sandwich ($17.3 \cdot 10^{-6}$ [4]) (figures 1-b and 2-b).

A flat non-active 33 mm wide edge must be added on both front and back sides in order to fit with the absorber (figures 1-c and 2-c). Connection pads (for signal collection and HV supply) will be etched, and connectors will be stapled on these edges.

Industrial constraints limit the useful width of polyimide¹ to 950 mm out of a 1000 mm wide sheet. The flat edges of electrode D are therefore to be limited in such a way to spare active area. This problem does not affect electrode C, given its smaller dimensions.

The four corners of both electrodes are notched in order to fit inside the mechanical structure (figures 1-d and 2-d) [5].

The position of each fold must be known with a 150 μm precision with respect to its closest neighbours. This position is determined by the mean of a hole at each fold extremity. During the folding procedure, these holes will house metallic pins, fixed on the folding table. The single bending knife will be fixed to the apparatus in such a way to achieve the folding on the axis between the location pins, which is the actual position of the fold. The holes will be drilled on an extra material added on the top and the bottom of each electrode² (figures 1-e and 2-e). The extra material will be cut away after the folding.

¹We use Kapton E (Dupont Corporation).

²For module 0, the electrodes will be delivered with etched crosses instead of holes. The drilling will be done elsewhere.

3 Design of the electrodes

The raw material for the electrodes as shown in figure 3 [1], consists of double-sided copper ($35 \mu m$) clad polyimide sheets ($50 \mu m$) plus a single-sided copper clad polyimide. After etching the internal copper layer, both sheets are glued together so as to have a Cu-Poly-Cu-Poly-Cu sandwich. Finally, the two external copper layers are etched. In this way, we obtain the desired physics parameters (granularity and samplings), routing facilities (connection lines, HV buses), and the mechanical requirements (fixation and bending holes).

The copper edge on the HV layer stops at $1 mm$ distance of the top and the bottom of the active volume defined in figures 1-b and 2-b. The signal layer ends at $1.250 mm$ so that the detecting area is well contained inside the volume in which the electric field is uniform. The copper of the extra material (for bending holes) starts at $0.5 mm$ distance from the end of the active volume, leaving $1.5 mm$ of polyimide without copper. This will facilitate cutting away the extra material after bending.

In z , the HV and the signal cells extend beyond the active volume by $2 mm$, on both flat edges. The remaining width of the flat edges will be used for signal connections, HV supply bus, and fixation holes. Non used copper area will not be etched away to strengthen the flat edges.

3.1 Samplings

Electrode D area is subdivided into three samplings. The first one (S1) extends till 6 radiation lengths (X_0) including all material in front of the active volume ($\sim 2X_0$). S2 stops at $24 X_0$ and S3 covers the remaining volume, except for $\eta < 1.5$, where S2 extends up to the end of the active volume. Electrode C has only two samplings, separated after $24 X_0$.

Theoretical separations between samplings are shown in figures 4-a and 5-a. The separations can cross folds, and thus, have to be shifted in order to insure a minimum distance of $2 mm$ between the fold curvature edge and the resistive ink edge (see next section). To facilitate the drawing, sampling separations must be computed by η steps (0.025 for S1/S2, 0.050 for S2/S3 and 0.100 for electrode C). The actual separations are shown in figures 4-b and 5-b.

Figures 6 and 7 show the actual number of radiation lengths before the end of each sampling [6], according to the actual separations.

The tighter granularity of S1 (electrode D) leads us to keep a $2 mm$ space between S1 and S2 on the HV layers. This distance is $1 mm$ for the signal layer. It insures a good signal collection efficiency while keeping the cross-talk at an acceptable level. The separation between S2 and S3 (and S1/S2 for electrode C) is 0.5 and $2 mm$ for HV and signal layers respectively.

The edges separations and the distances between samplings are summarized in table 1.

| quantity | distance in electrode C [<i>mm</i>] | distance in electrode D [<i>mm</i>] |
|---|--|--|
| kapton-HV layer edges (low and high η) | 1 | 1 |
| kapton-signal layer edges (low and high η) | 1.25 | 1.25 |
| S1/S2 HV sep. | 0.5 | 2 |
| S1/S2 signal sep. | 2 | 1 |
| S2/S3 HV sep. | none | 0.5 |
| S2/S3 signal sep. | none | 2 |
| S1 HV cell sep. | 1 | 0.5 |
| S1 signal cell sep. | 1.5 | 1 |
| S2 and S3 HV cell sep. | 1 | 1 |
| S2 and S3 signal cell sep. | 1.5 | 1.5 |

Table 1: Edges, samplings and cells separation distances.

3.2 Granularity

Each sampling is etched into projective cells along the η direction according to physics needs. The basic requirement for granularity is $\Delta\eta = 0.025/8$ for S1, 0.025 for S2 and 0.050 for S3. These numbers have been tuned to cope with the end-cap specificities: for intermediate regions ($\eta < 1.5$ and $2.4 < \eta < 2.5$), where the amount of dead material has its maximum, the S1 granularity is reduced to $\Delta\eta = 0.025$.

For $1.8 < \eta < 2.4$, the S1 strip pitch would be below 5 *mm* if the cell size is kept at $\Delta\eta = 0.025/8$, which is difficult to achieve in industry. Thus, the granularity in this region has been optimised to keep a minimal pitch of 5 *mm*. The final granularity is given in table 2. A coarser granularity ($\Delta\eta = 0.100$) is used for both samplings of electrode C.

| η | S1 | S2 | S3 |
|----------------------|---------|-------|-------|
| $1.375 < \eta < 1.5$ | 0.025 | 0.025 | none |
| $1.5 < \eta < 1.8$ | 0.025/8 | 0.025 | 0.050 |
| $1.8 < \eta < 2.0$ | 0.025/6 | 0.025 | 0.050 |
| $2.0 < \eta < 2.4$ | 0.025/4 | 0.025 | 0.050 |
| $2.4 < \eta < 2.5$ | 0.025 | 0.025 | 0.050 |
| $2.5 < \eta < 3.2$ | 0.100 | 0.100 | none |

Table 2: Granularity of the end-cap electrodes in η direction.

The distance between neighbouring HV cells is 0.5 *mm* in the first sampling of the D electrode, to take advantage of the fine granularity, and is 1 *mm* elsewhere. The cells of the HV layers extend beyond their corresponding signal cell by 0.250 *mm* in η direction, leading to a separation between signal cells larger by 0.5 *mm*. This small difference can make up for a small relative misalignment between the three conductive layers. Table 1 gives the separation widths between cells.

Connection lines for signal read-out and HV supply of the middle sampling (S2) of electrode D are added to the design. These services are brought to S2 from the front edge for $\eta < 1.5$ and from the back elsewhere. Connection lines are needed also for electrode C in order to have the services on the back side for both samplings. The width of the connection lines is optimised in order to have an acceptable inductance (see next section).

Figures 8 and 9 show the projective cell drawing of the signal layer. The HV layers are the same, except for cells and samplings separation, and for the top and bottom borders as specified above. The notches in the separations between S1 and S2 in electrode C, and S2 and S3 in electrode D seen in figures 8 and 9 are there to insure the 0.250 mm containment of the signal cells inside the HV ones under the inter-samplings resistors region (see next section).

3.3 Routing facilities

Each electrode cell has to be connected to the HV supply and its signal has to be transmitted to the read-out system.

For the read-out signals, there is a connection line from each cell to the front or back flat areas. The line continues on some printed path which groups sets of cells exiting on female contacts³ which are stapled and soldered to the electrode material and grouped onto connectors with protective sleeves. Appropriate holes were drilled in the polyimide to bring the signal lines to the surface. Outside the electrode, the signals go through summing boards, motherboards, cold cables, feedthroughs until they reach the read-out electronics which are located just after the cryostat exit.

The high voltage from the HV power supplies outside the detector enters the cryostat through special HV feedthroughs, continues *via* cold cables, and connects to HV boards which are plugged onto the connectors at the electrode edge. From there, the HV has to be distributed to each cell through HV buses, feed resistors (two silk screened resistors of 1 M Ω in parallel for each HV cell), connection paths and further lines to reach the middle sampling. The HV distribution is kept completely independent on each side of the cells, leading to different paths, pins and connections for each HV side. Figure 10 shows details of signal and HV line paths on the backward flat area of electrode D.

Following guidelines were used for the implementation of the routing :

- Connector placement compatible with absorber support structure and simplification of the associated motherboards.
- Compatibility of connectors with the ones used on the barrel for cost reduction where possible.
- Cross-talk minimization, especially via HV buses.
- Connection line widths compatible with inductance and capacitance requirements.
- Minimization of cell size reduction due to routing.
- Displacement of silk screened resistors away from folding regions.

³We use Nicomatic female contacts Ref. 10025.

- Guaranteed HV-signal and HV-ground separations.
- Standard output pin pitch : 2.54 mm for the front connectors, $2 \times 2.54\text{ mm}$ for the back connectors where the pin density is lower.

The routing and final plots including all layers and all cells were performed using the Autocad v.12 software.

The connector drawings on the electrodes can be seen in figures 11 and 12.

3.4 Ground contacts

The drift electric field between the absorber plates and the HV electrode planes is obtained by applying a DC voltage to the HV planes, while the absorbers are grounded. This ground potential is the reference for both the HV supplies and the read-out system. Thus it has to be connected electrically all the way from the absorbers to the preamplifiers.

As the absorbers have no electrical connections, these have to be made by means of connectors and cabling linked to the electrodes. At least one ground pin (two in most cases) is foreseen for each signal connector from where electrical ground is carried up to the read-out electronics. These pins are connected with specific copper pads drawn on the flat edges. The absorbers have to be connected with these grounding pads, bridging the few mm liquid argon gap.

The barrel method (Cu-Be springs soldered on the electrodes) is only in a very difficult way applicable to the end-cap, as one would need many springs of several different nominal heights, to cope with the gap variation along the radius.

The ground contact will be carried by a single-sided copper (or gold plated copper) polyimide sheet (called “flap” in the following), put across the gap. The copper touches the absorber on one area while it is soldered to the electrode ground pads on the other side. The flap is held against the absorber by the spring effect of a pure kapton tube which is compressed across its diameter.

Several diameters (7 different) of the tubes have been chosen, so that the tubes are only slightly (fraction of a mm) compressed at the side where the gap is thinner, and almost not compressed where the gap is larger. There, we use the rigidity effect of the flap itself, partially held down by the absorber bars to insure the electrical contact. Tubes and flaps are glued together, and the set is soldered onto the electrodes. Such a setup is shown in figure 13.

The copper on the flap is engraved in such a way that the part in contact with the absorber is full copper, while only thin paths carry the contact towards the electrode. This prevents a full copper surface directly above signal paths which would cause large cross-talk.

The advantage of this approach is that the contact area on the absorbers is much longer than with springs. One set “flap-tube” has to be soldered on each side, to ground the two absorbers above and below the electrode as can be seen from figure 13 (right photo). Twelve different sets are needed, 4 on the large electrodes back side, 6 on the front side and 2 on the small electrodes. Details on gaps and tubes dimensions are shown in table 3. The two soldered flaps of a given connector (one for each side) are not identical but symmetric.

Some prototypes of this construction have been achieved. The principle was successfully tested, in the air and inside liquid nitrogen, where contact resistances under $100\text{ m}\Omega$ were

obtained.

| Flap type | Min gap [<i>mm</i>] | Max gap [<i>mm</i>] | Flap-Tube length [<i>mm</i>] | Tube ϕ [<i>mm</i>] |
|-----------|--------------------------|--------------------------|-----------------------------------|------------------------------|
| F1 | 5.1 | 5.6 | 133 | 5.6 |
| F2 | 4.5 | 5.0 | 112 | 5.0 |
| F3 | 3.8 | 4.4 | 148 | 4.4 |
| F4 | 2.9 | 3.7 | 211 | 3.7 |
| F5 | 2.1 | 2.7 | 147 | 2.7 |
| F6 | 1.4 | 2.0 | 148 | 2.0 |
| B1 | 5.0 | 5.9 | 213 | 6.0 |
| B2 | 4.5 | 5.0 | 120 | 5.0 |
| B3 | 3.3 | 4.2 | 208 | 4.4 |
| B4 | 1.7 | 2.7 | 243 | 2.7 |
| S1 | 4.9 | 6.0 | 97 | 6.0 |
| S2 | 3.6 | 4.8 | 97 | 5.0 |

Table 3: 12 types of flaps with spring tubes of 7 different diameters.

3.5 Fixation and bending holes

Fixation holes are made on the flat edges to allow the precise location of the electrodes on the absorber bars. The main fixation holes (circular) are drilled close to the $\eta = 2.5$ gap between the outer and the inner wheel to insure a precise knowledge of the gap position (figures 14 and 15).

Bending holes are also shown in figures 14 and 15. They are placed on concentric circles to keep a constant distance between the bending machine indexation pins. The T shape avoids having to cut in a curved region, after the bending.

The 950 *mm* limitation of the width of useful polyimide prevents the implementation of the bending holes for the most external folds of electrode D. The closest holes will be used to perform the folding.

4 Electrical properties

4.1 Channel capacitance

Since the signal collected on the electrode is a capacitive induced current generated by the drifting charges inside the liquid argon gaps, the capacitance of each channel is a very important parameter for calorimeter calibration.

The capacitances were computed and are shown in figures 16 and 17. The signal summing in azimuth (12 electrodes for S1, 3 for S2 and S3 for electrode D, 4 for electrode C), and the edge effects have been taken into account. The cross-talk between neighbouring channels was not considered. This effect can be important for the strips (first sampling of electrode D).

4.2 Connection lines inductance

The width of connection lines of S1 (S2) of electrode C (D) must be as thin as possible, in order not to spoil the efficiency of the sampling they go through. On the other hand, thin lines add inductance to the read-out channel. This inductance must be kept below 20 nH , and be as constant as possible.

It has been found that a constant width of 2.5 mm for the signal connection lines gives a nearly constant inductance value of about 17 nH over the whole pseudorapidity range of the outer wheel lines and 13 nH for the inner wheel ones (figures 18 and 19). This is naturally achieved in the end-cap because the inductance increases as the product between the line length and the liquid argon gap ($l \cdot g$). Since the increase of l is nearly compensated by the decrease of g with η , the inductance remains constant for a constant line width.

The width of the HV connection lines is set to 3 mm , to keep the 0.250 mm containment of signal cells inside the HV ones.

4.3 Protection resistors

Accidental sparks may occur on HV layers, and induce large currents that can damage the preamplifiers. To minimize this effect, HV cells (except for strips) are divided into small pads along the z direction, interconnected by silk screened resistors (figure 20). The resistance value is determined by the geometry of the slit between the two copper pads, given the value of $1\text{ M}\Omega/\square$. All the resistance values reported in this note are at liquid argon temperature, and have to be divided by a factor ~ 3 to obtain their values at room temperature [7]. Those slits are kept on the flat side of the folds, and are staggered in order not to create mechanical weak regions that might tear the electrodes (figures 21 and 22). The protection of the preamplifiers requires high resistance values to attenuate possible large currents.

On the other hand, pile-up of minimum bias events will continuously create charges inside the liquid argon gaps, and thus, induce a permanent current on the high voltage lines. To minimize high voltage drops, this current must go through small resistances.

There are also resistors between samplings, to insure a proper HV routing for all cells. Their value is $1\text{ M}\Omega$ except for the strips (between S1 and S2 for electrode D) where it varies between 0.4 and $0.8\text{ M}\Omega$, depending on strip pitch. These resistances must be added to the protection and polarization resistors to obtain the total resistance seen by the HV supplies.

A compromise that keeps the high voltage drop below 0.6% ⁴ and satisfies the preamplifiers protection needs has been worked out. The calorimeter response to minimum bias events was simulated. The permanent current seen by each HV supply unit [8] together with the nominal high voltage value used in simulation [9] is shown in table 4.

Values of resistors, and their number were optimised for the worst case: we assume that charges are created in the beginning of active volume and have to cross all resistors (polarization, protection and inter-samplings). This may explain the disagreement with the analytical calculation of signal loss in [10] where sampling 3 resistors were not taken into account, which is more realistic since sampling 2 is fed in parallel from the HV bus and through sampling 3. Another point is that the hadronic part of the pile-up energy loss is deposited all along

⁴This leads to a relative signal loss below 2 per mil.

the particle path inside the calorimeter, not in the beginning as in our estimation. Thus our computation is pessimistic, allowing the HV supply system to withstand large pile-up fluctuations.

To obtain low resistances, the slit width has been changed from 3 to 1.5 *mm* beyond $\eta = 1.6$, and one resistor out of two has been removed beyond $\eta = 2$.

The maximum resistance value seen by any HV channel (after optimisation) for each HV supply region, on each HV plane is shown in table 4, together with the HV drop fraction. These drops were computed by taking into account the number of HV planes⁵ fed in parallel by one HV supply (24 in the outer wheel, 16 in the inner one).

Table 4 shows that our scheme does not satisfy the 0.6 % drop requirement in the high voltage value in the inner wheel, if we keep the HV configuration as described in [9]. The preamplifiers would not withstand a lower resistance value, and the current is higher than the HV supply limit (0.2 *mA*). Therefore it was decided to increase the number of HV supplies of the inner wheel by a factor 4. Each supply will feed 4 HV planes. The currents of the two last lines of table 4 must be divided by 4.

| η | V [V] | I [μA] | R_{max} [$M\Omega$] | ΔV [%] |
|----------------------|---------|-----------------|-------------------------|----------------|
| $1.375 < \eta < 1.5$ | 2500 | 4 | 6.3 | 0.04 |
| $1.5 < \eta < 1.6$ | 2300 | 10 | 6.2 | 0.11 |
| $1.6 < \eta < 1.8$ | 2100 | 26 | 3.6 | 0.19 |
| $1.8 < \eta < 2.0$ | 1700 | 33 | 3.1 | 0.25 |
| $2.0 < \eta < 2.1$ | 1500 | 18 | 3.4 | 0.17 |
| $2.1 < \eta < 2.3$ | 1200 | 37 | 3.4 | 0.44 |
| $2.3 < \eta < 2.5$ | 1000 | 38 | 3.7 | 0.59 |
| $2.5 < \eta < 2.8$ | 2250 | 212 | 2.0 | 1.18 |
| $2.8 < \eta < 3.2$ | 1750 | 273 | 2.0 | 1.95 |

Table 4: Nominal high voltage, pile-up current, maximum resistance and maximum high voltage drop for each HV supply region before modification of the inner wheel HV distribution scheme.

5 Conclusions

Large multi-layer copper-polyimide electrodes have been designed and will be used in the ATLAS end-cap electromagnetic calorimeter. Several compromises have been worked out between physics requirements and technical possibilities. Splitted views of the two electrodes type can be seen in figures 23 and 24. More detailed drawings can be loaded from [11].

⁵1 electrode = 2 HV planes.

Acknowledgments

This work was achieved thanks to the support provided by the CPPM-Marseille mechanics team. Many thanks to P. Dargent, P. Karst, L. Martin, J.L. Gimenez, L. Lopez and P.E. Blanc. We wish to thank also O. Martin (CPPM) and S. Simion (CEA-Saclay) who provided simulation results for parameter optimisation. We would like to express our gratitude to N. Séguin-Moreau (LAL-Orsay) who helped in electrical computations, and to our colleagues from the barrel group S. Jezequel, B. Aubert (LAPP-Annecy), C. Costa, M. Mazzanti (INFN-Milano) and B. Canton (LPNHE-Paris VI) who shared their experience with us.

References

- [1] ATLAS liquid argon calorimeter TDR, CERN/LHCC/96-41.
- [2] B. Aubert and C.P. Marin, technical specifications for large size signal electrodes, CERN/IT-2447/PPE.
- [3] L. Martin, J.L. Gimenez, A. Chekhtman, CPPM-ATLAS internal report ABS.YYY.00.DRa.3.
- [4] P. Dargent and S. Jezequel, private communications.
- [5] See <http://marpix1.in2p3.fr/calor/mechanics/STR-Structure> and drawings there in.
- [6] O. Martin, E. Monnier and S. Tisserant, ATLAS-LARG-47/Nov. 96.
- [7] M. Mazzanti, private communication.
- [8] S. Simion, private communication.
- [9] ATLAS calorimeter performance TDR, CERN/LHCC/96-40.
- [10] W. Bonivento, ATLAS-LARG-81/Sep. 97.
- [11] See <http://marpix1.in2p3.fr/calor/instrum/KAP-Kaptons> and drawings there in.

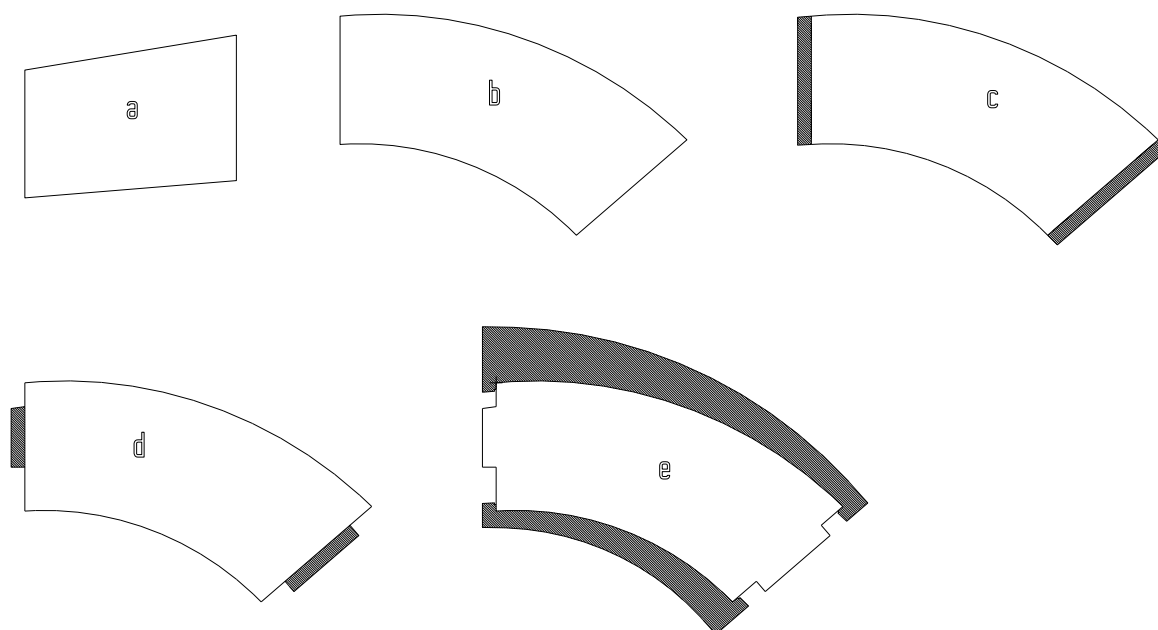


Figure 1: External geometry of the C electrode: a) active volume (folded), b) active volume unfolded, c) with the flat extension (dark), d) with mechanical notches, e) with the extension for folding holes.

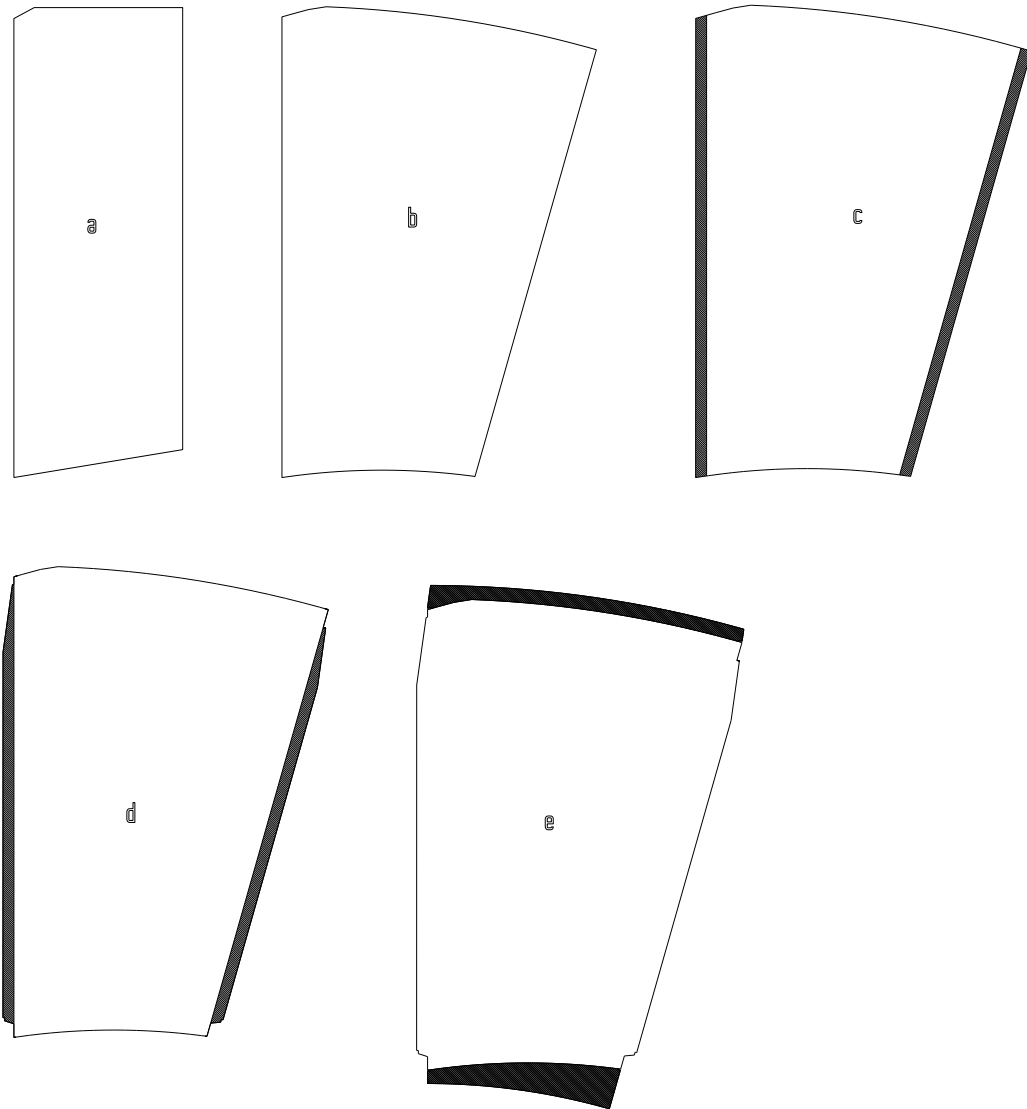


Figure 2: External geometry of the D electrode: a) active volume (folded), b) active volume unfolded, c) with the flat extension (dark), d) with mechanical notches, e) with the extension for folding holes.

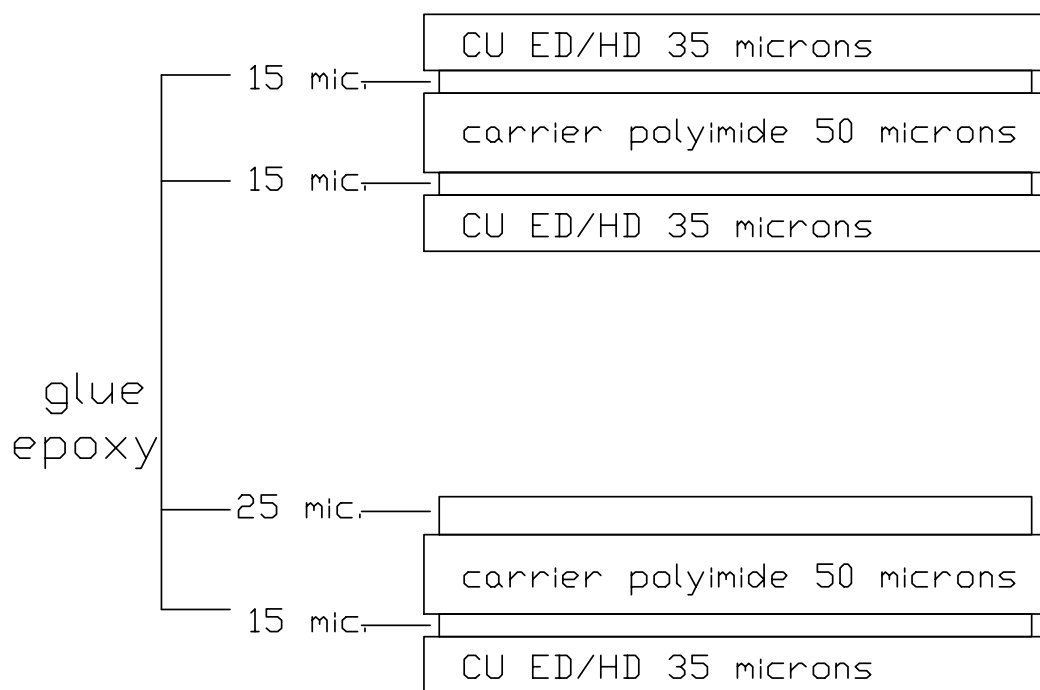


Figure 3: Electrode sandwich structure.

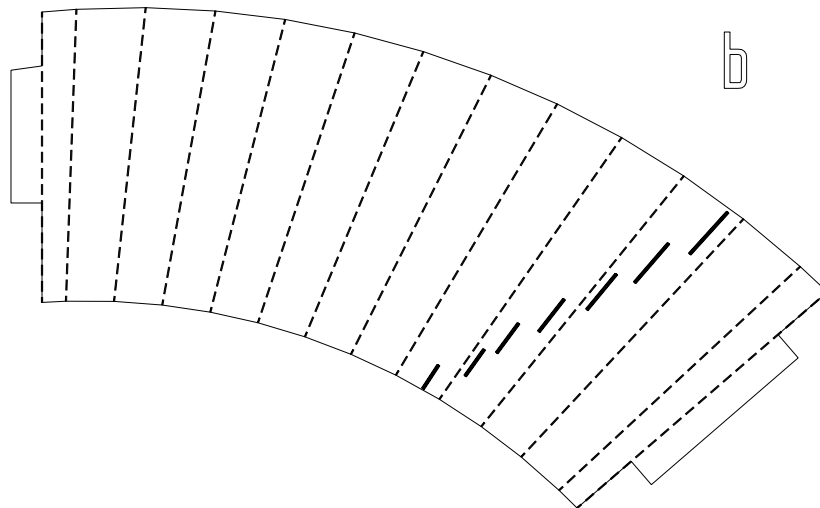
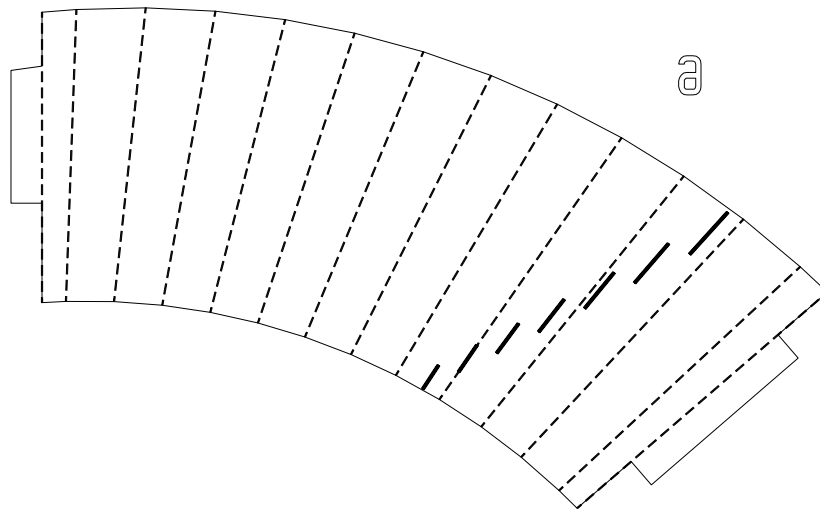


Figure 4: Sampling separation in electrode C: a) nominal, b) actual. Thick lines are the separations and dashed thin lines are the folds.

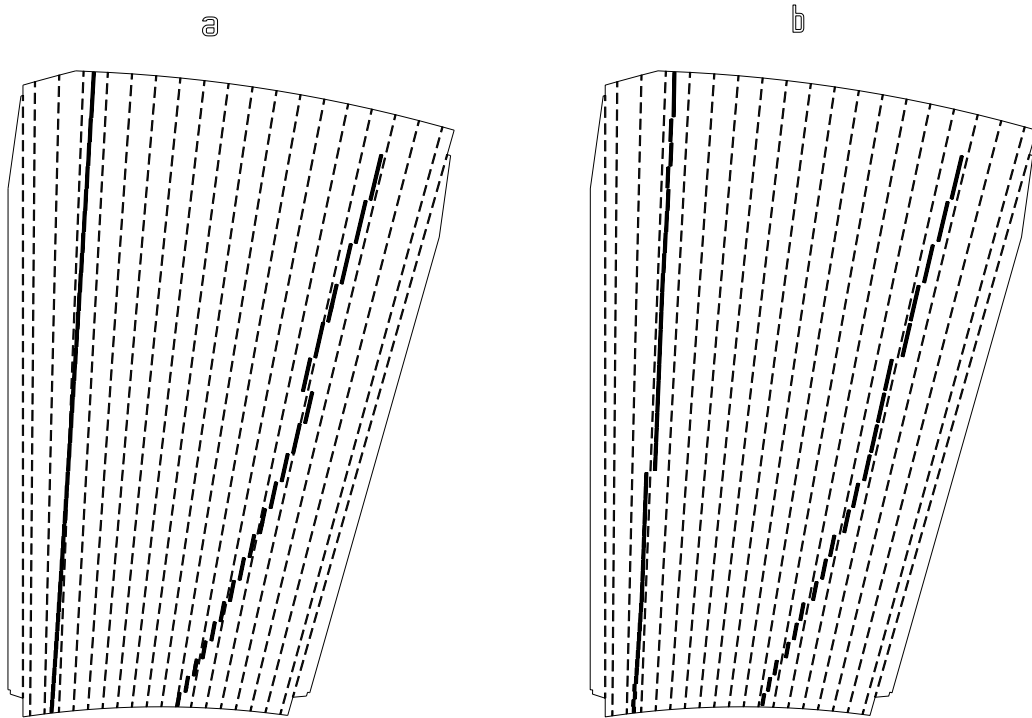


Figure 5: Sampling separation in electrode D: a) nominal, b) actual. Thick lines are the separations and dashed thin lines are the folds.

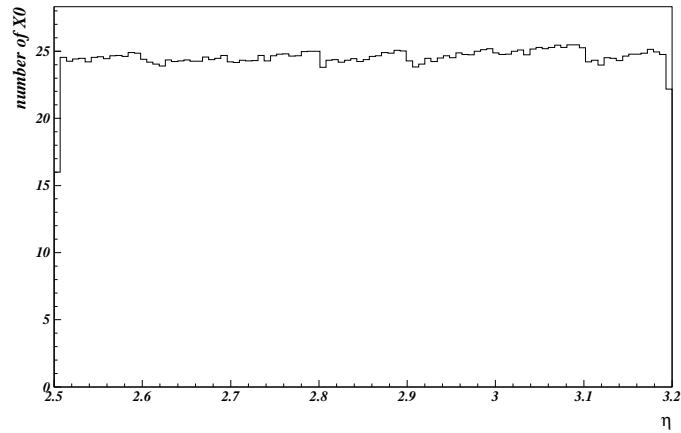


Figure 6: Actual number of radiation lengths at the end of sampling 1 of electrode C.

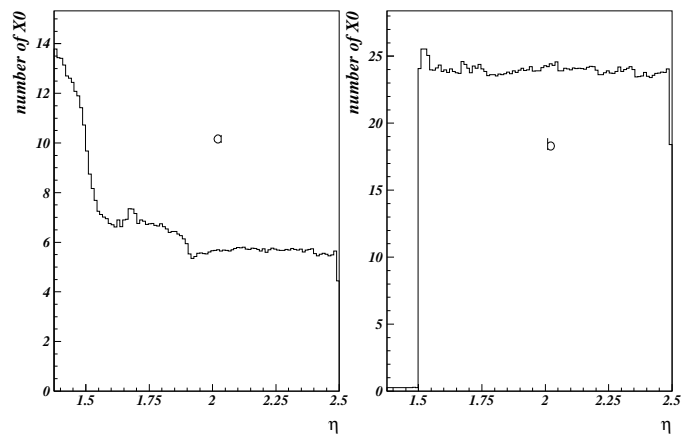


Figure 7: Actual number of radiation lengths at the end of: a) S1, b) S2 of electrode D.

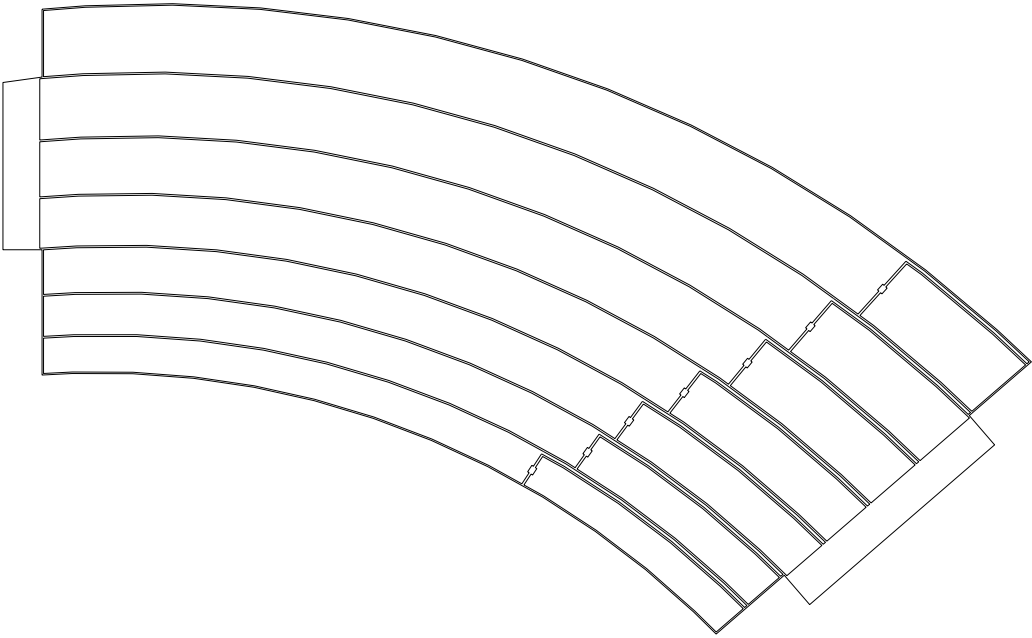


Figure 8: Copper signal layer of electrode C.

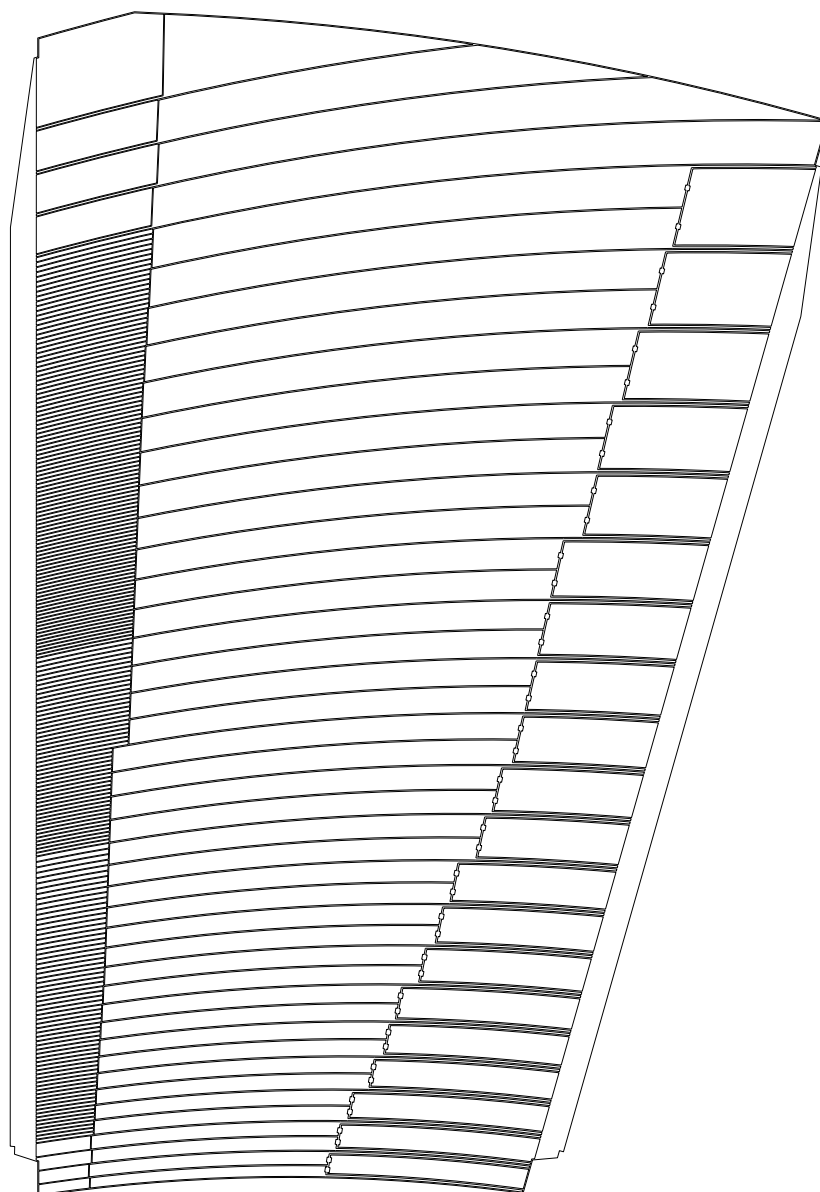


Figure 9: Copper signal layer of electrode D.

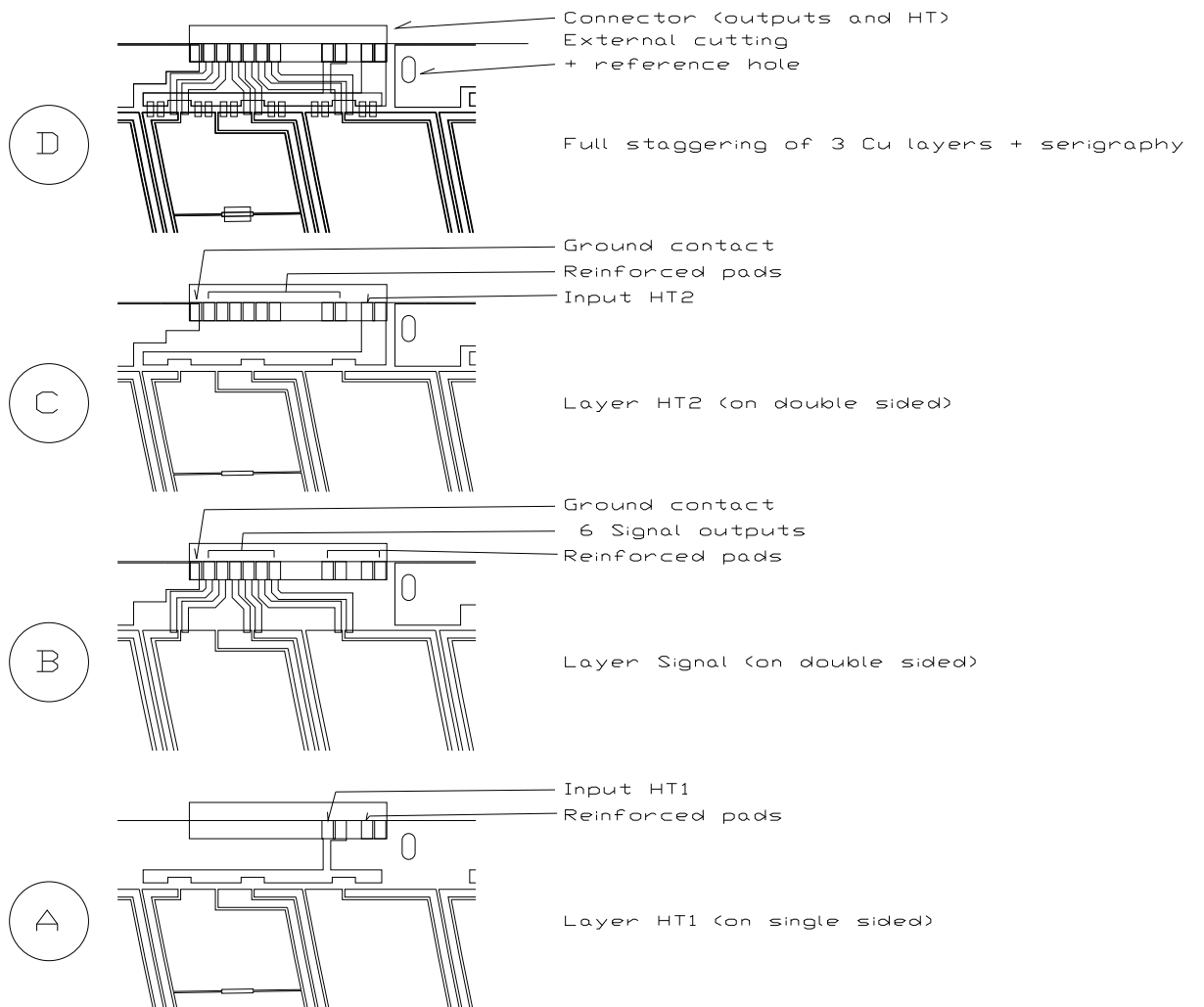


Figure 10: HV supply lines details (A and C), signal transmission lines (B) and the full view of the three layers (D).

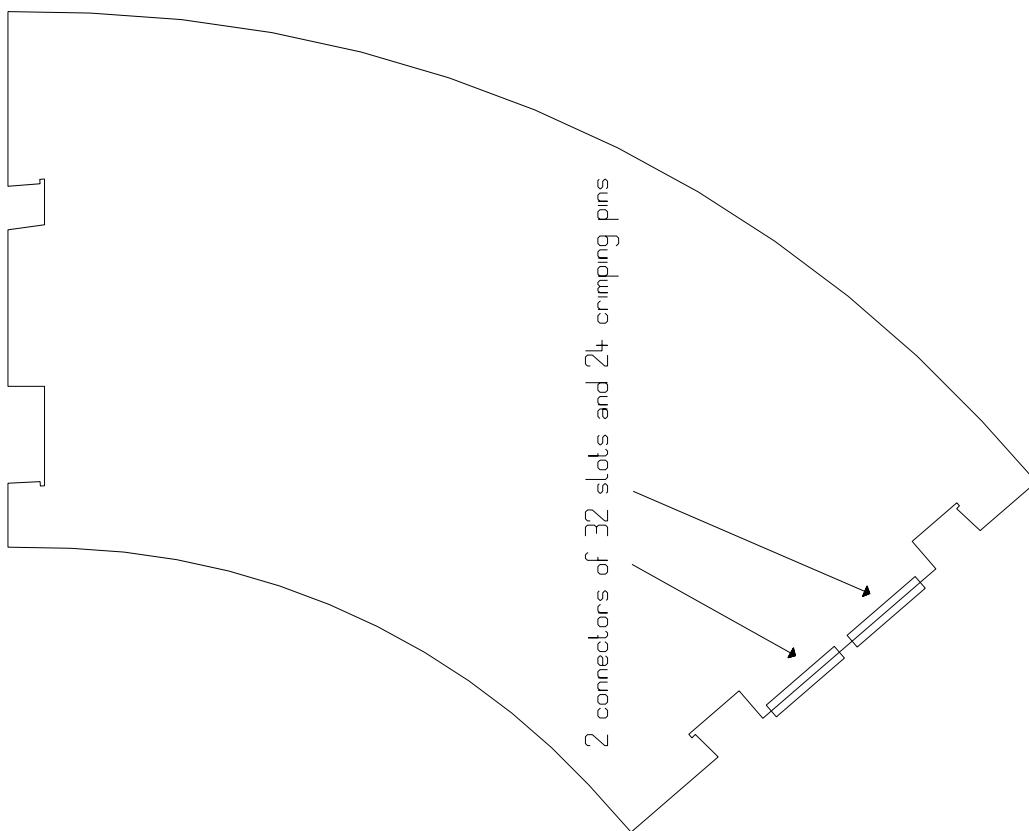


Figure 11: Connectors of electrode C.

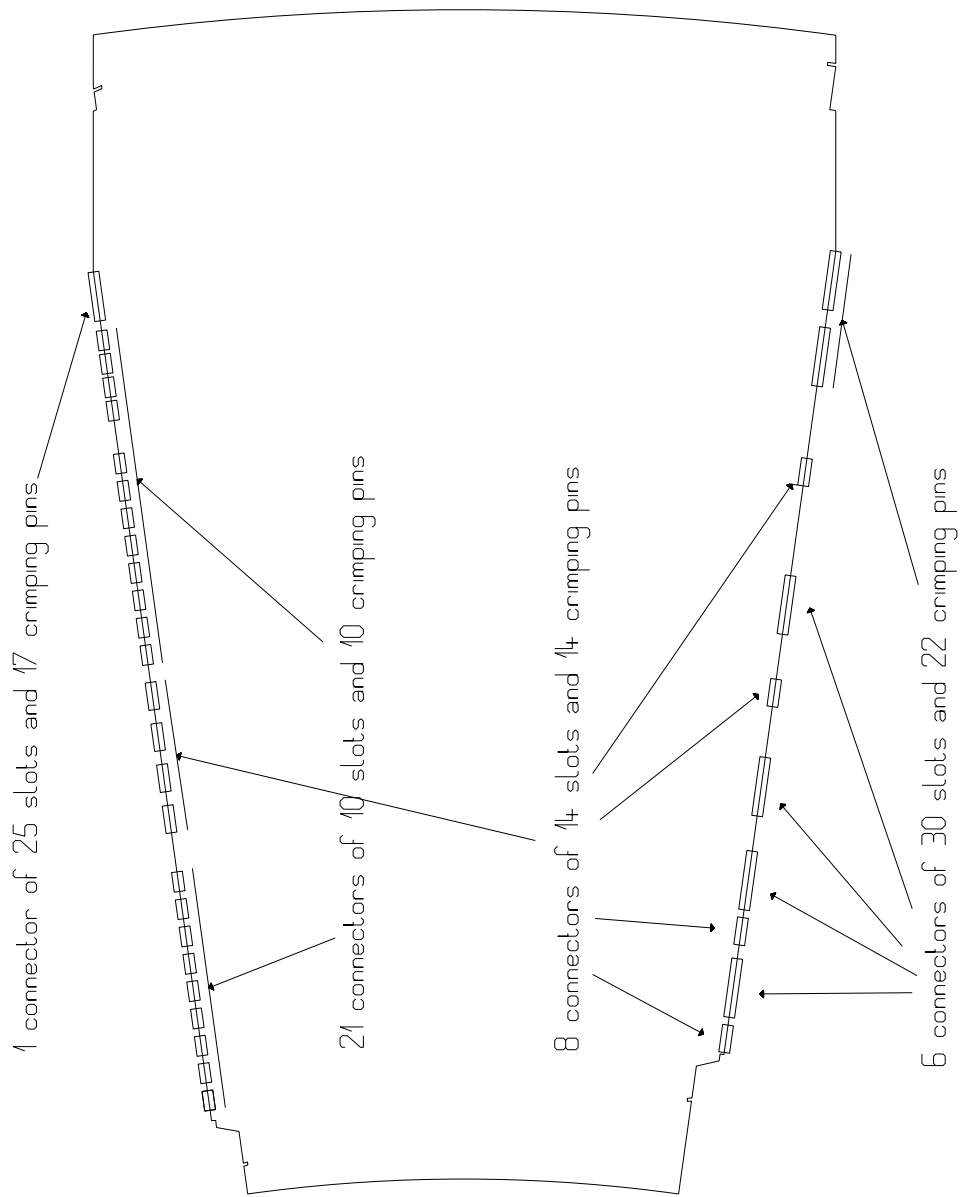


Figure 12: Connectors of electrode D.

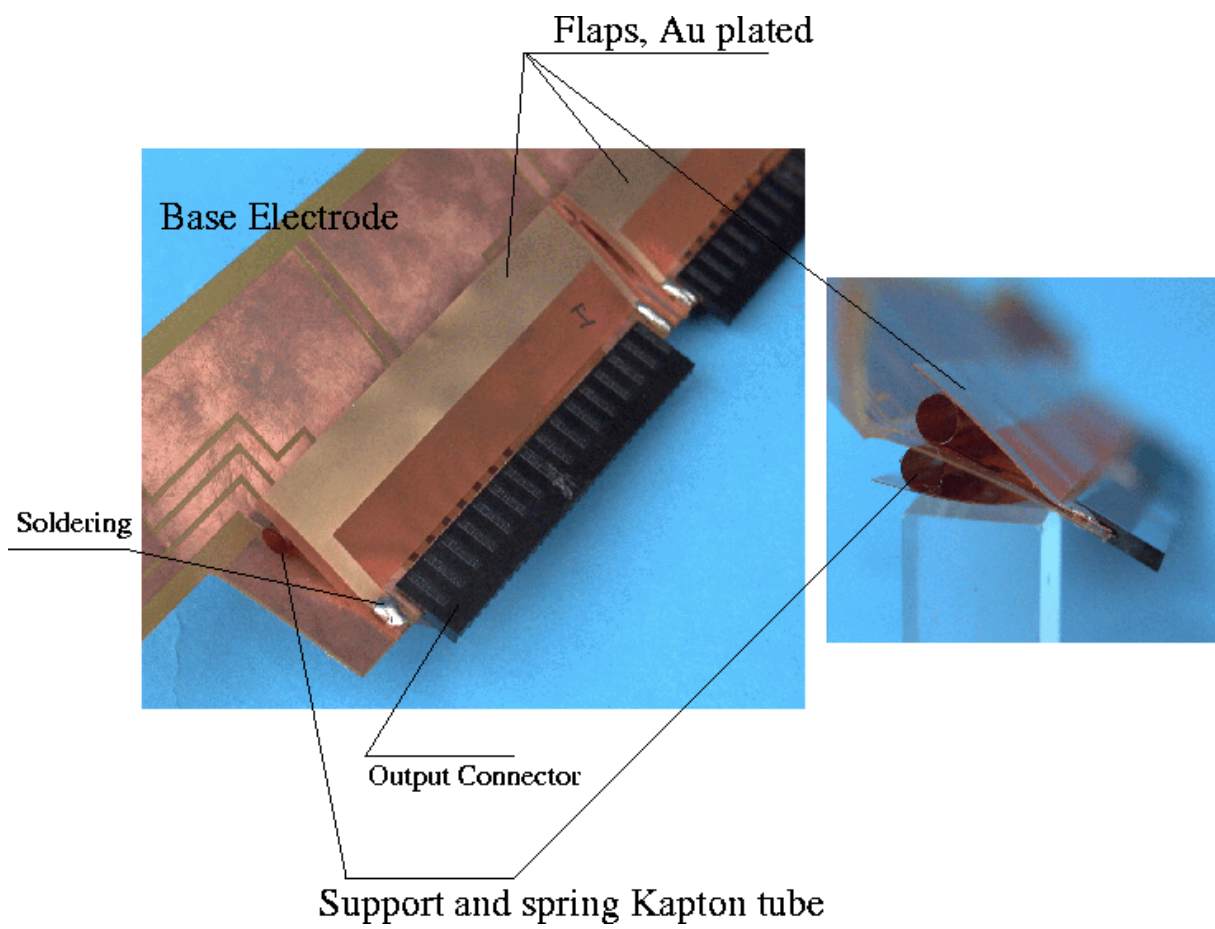


Figure 13: Ground contact scheme: top view (left) and side view (right).

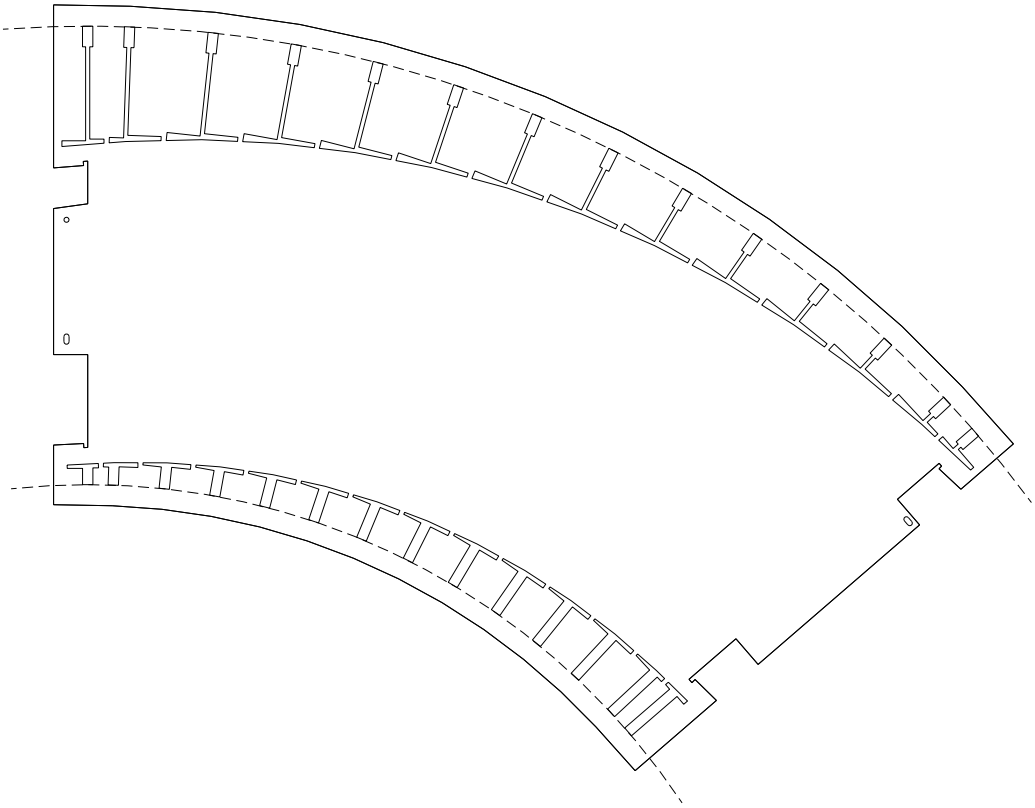


Figure 14: Fold location and fixation holes of electrode C.

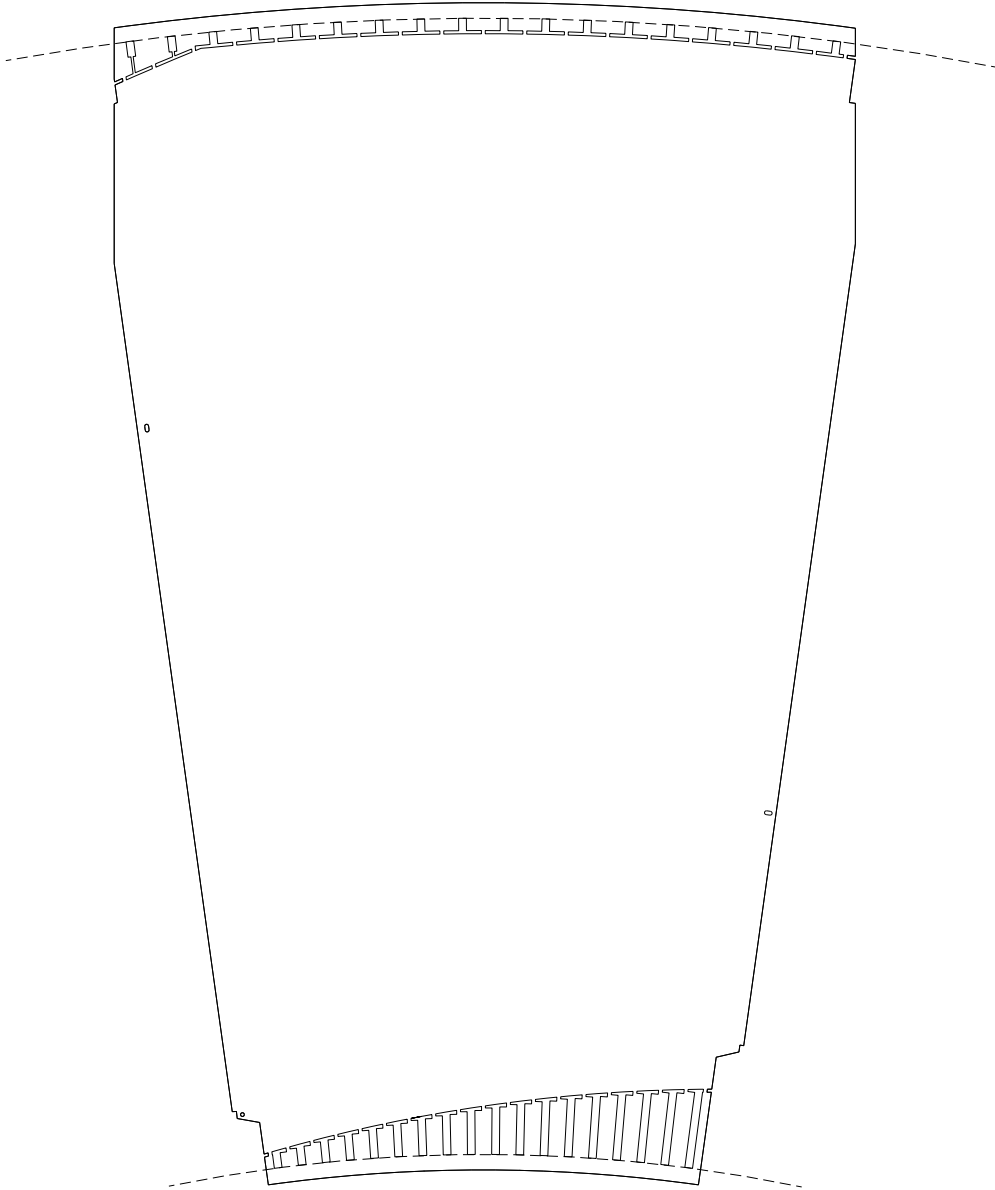


Figure 15: Fold location and fixation holes of electrode D.

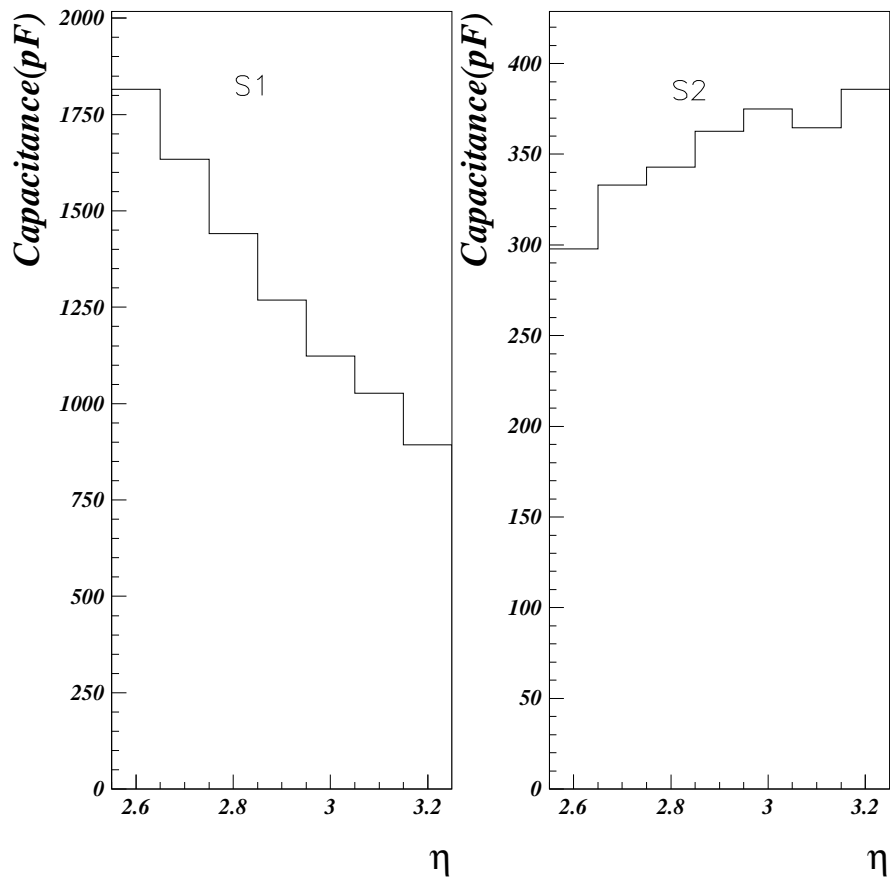


Figure 16: Capacitance of read-out channels of the 2 samplings of the inner wheel.

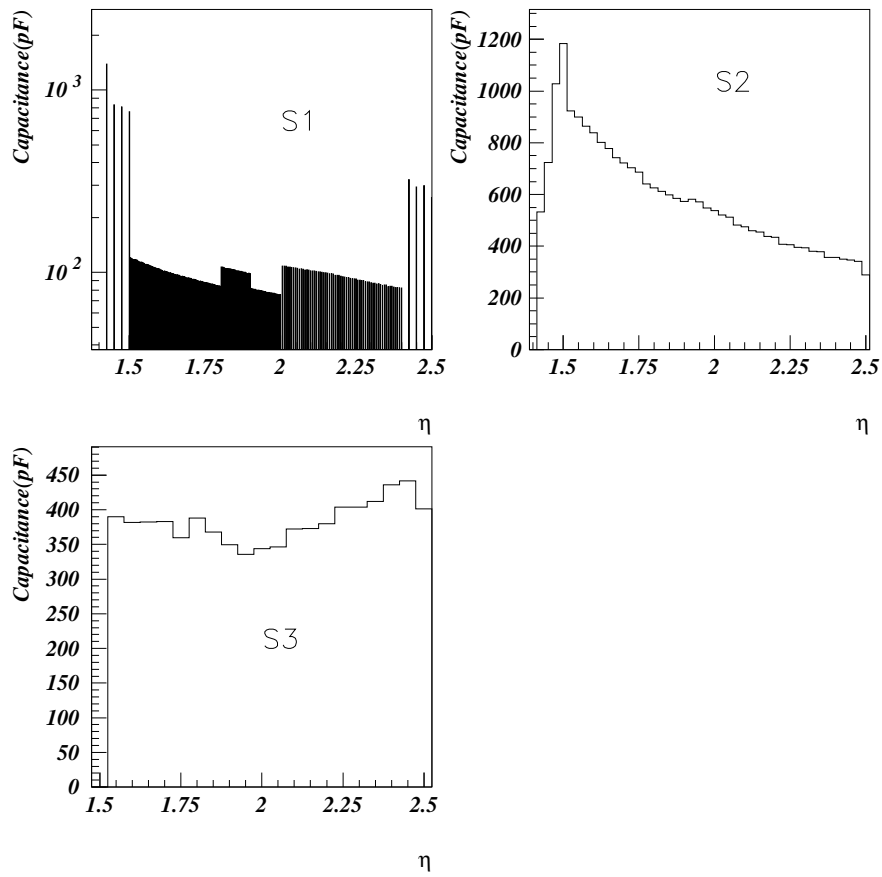


Figure 17: Capacitance of read-out channels of the 3 samplings of the outer wheel.

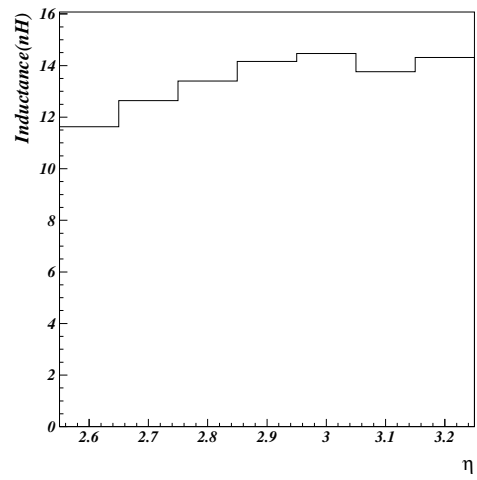


Figure 18: Inductance of connection lines of the first sampling of electrode C.

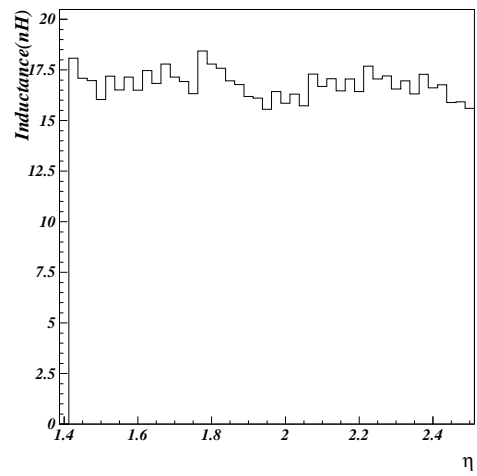


Figure 19: Inductance of connection lines of the second sampling of electrode D.

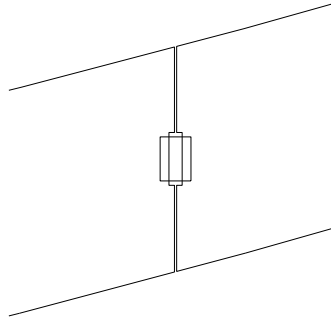


Figure 20: Two pads of a HV channel connected by a silk screened resistor.

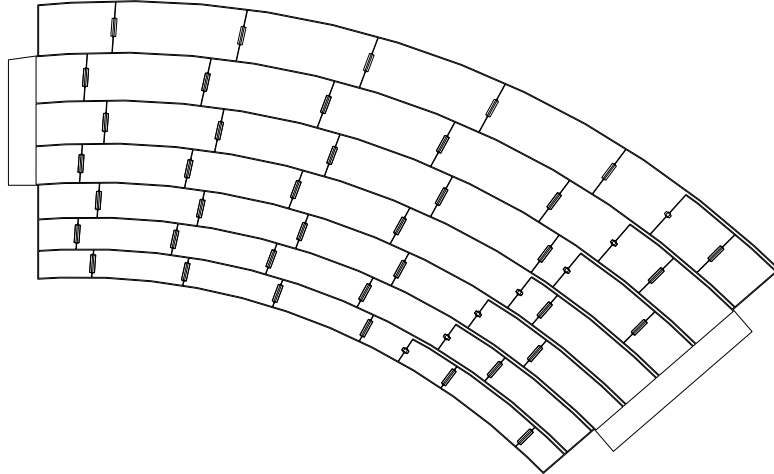


Figure 21: HV layer of electrode C with its resistors.

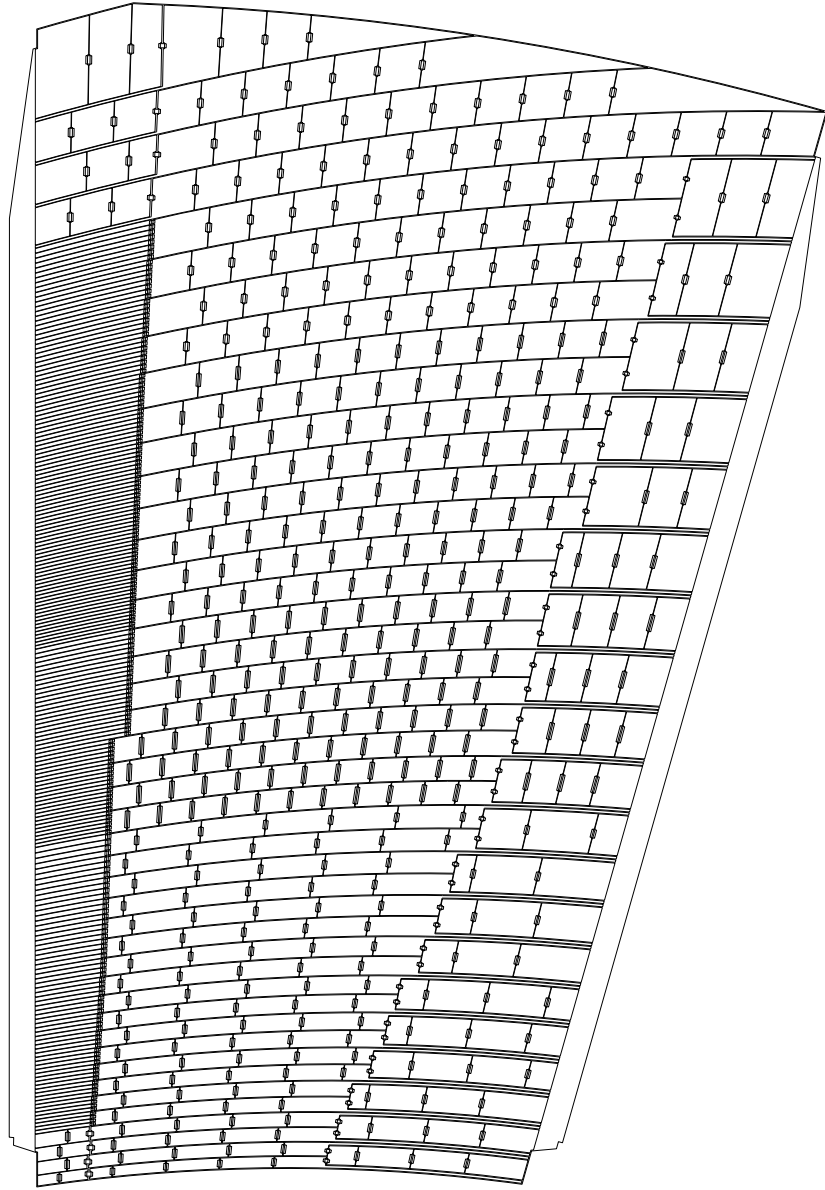


Figure 22: HV layer of electrode D with its resistors.

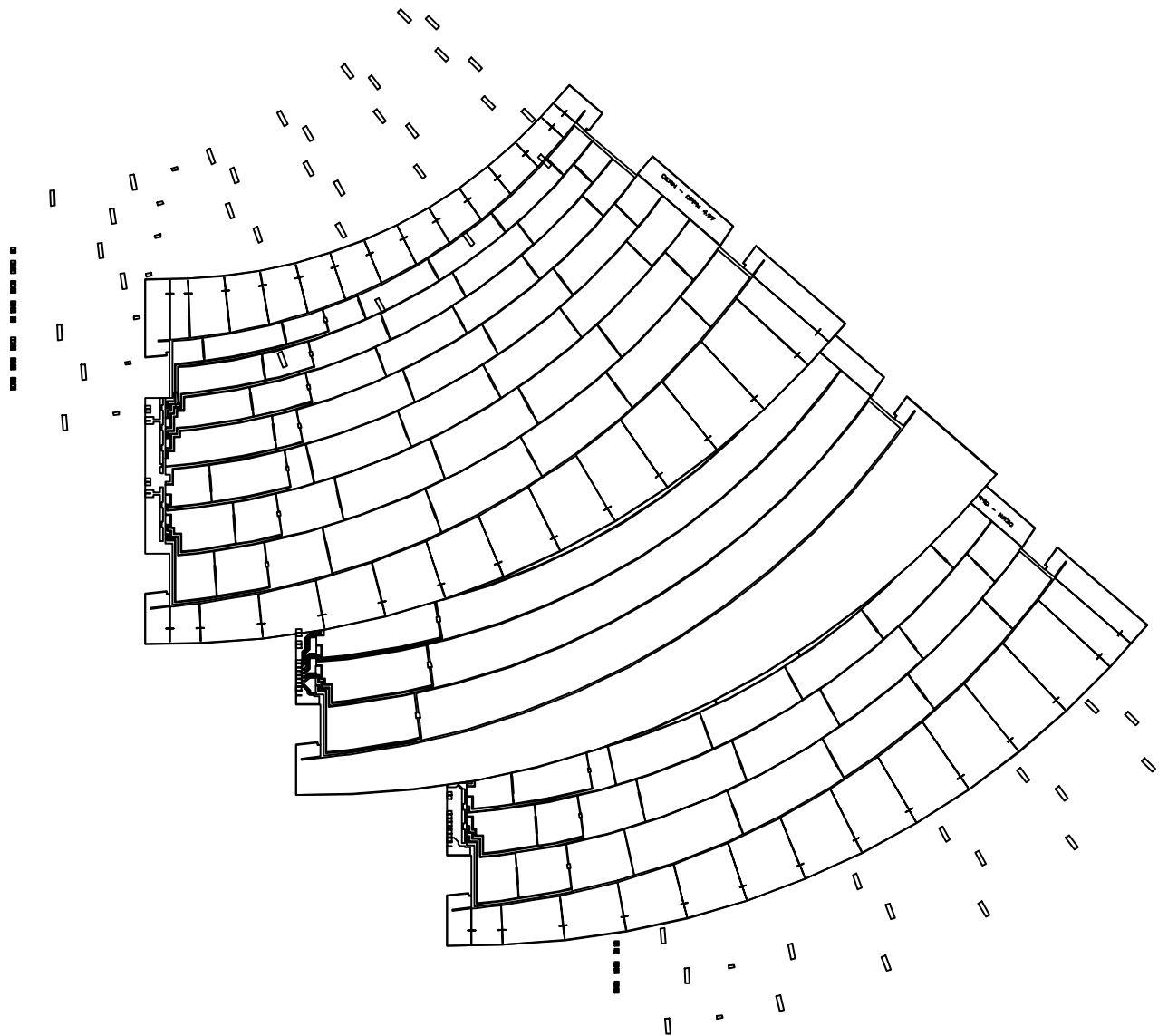


Figure 23: Split view of electrode C (For clarity, only part of the resistor layer is drawn here).

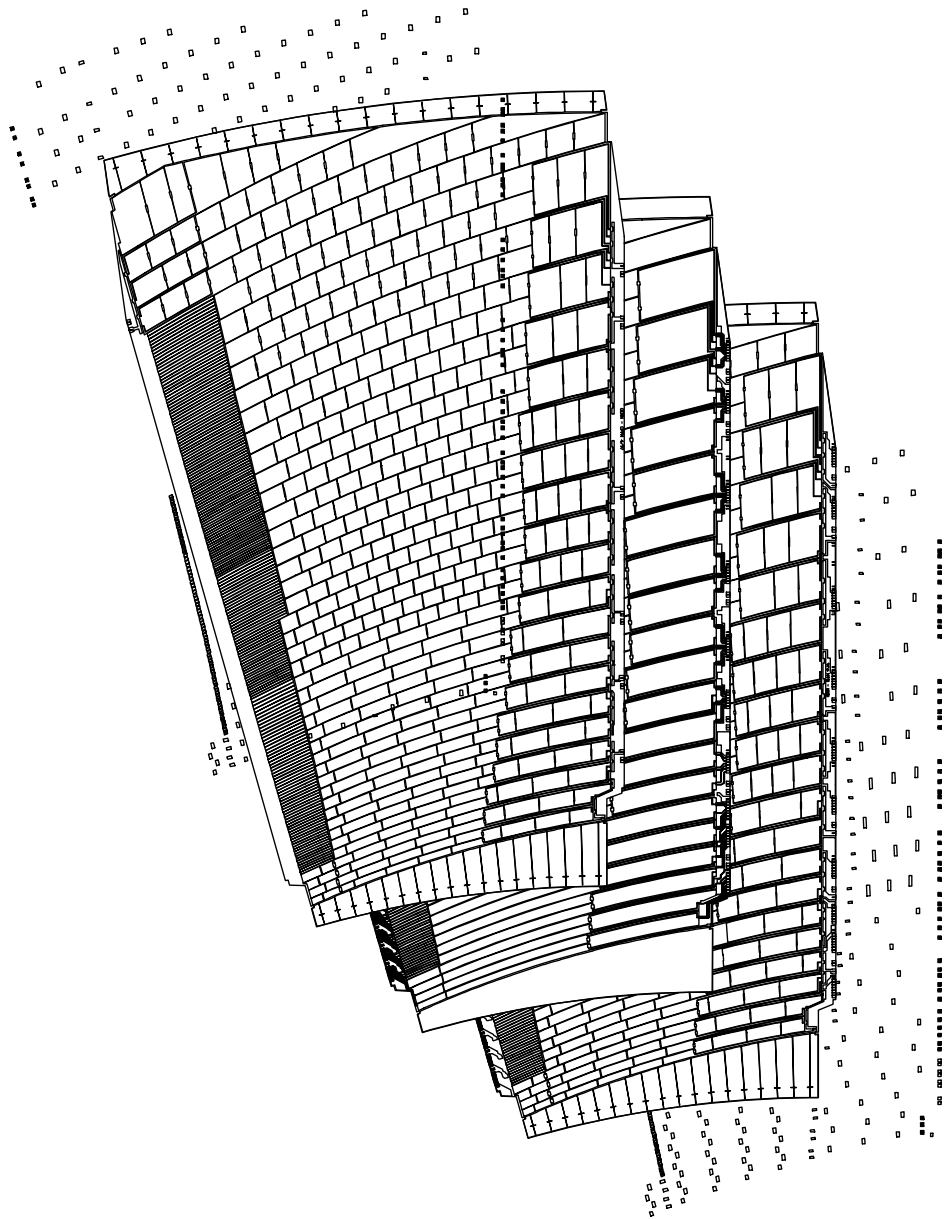


Figure 24: Splitted view of electrode D (For clarity, only part of the resistor layer is drawn here).